Remote-sensing of wave transformation in the surf zone

Kévin Martins[1], Chris E. Blenkinsopp[1], Erwin W. J. Bergsma[1], Hannah E. Power[2], Brittany Bruder[3], Jack A. Puleo[3]

Abstract

Skewness and asymmetry in nearshore cross-shore current velocities play an important role in the movement of sand. In the surf zone, the increasing non-linearities in the wave shape due to the decreasing depth lead to non-linearities in the bottom current velocities, and influence the beach morphology by balancing the undertow effect in transporting sand offshore. However, *in-situ* measurements of current velocities are difficult to obtain in such energetic conditions as those found in the surf zone. Remote-sensing technology and LiDAR scanners in particular offer the possibility to measure the surface elevation without having to interact with it. In this paper, the datasets from three LiDAR scanners obtained during the WASH experiments are used and compared to *in-situ* hydrodynamic data. The objective is to investigate the relation between third-order moments (asymmetry and skewness) obtained at the surface to that at the bottom in the underlying current velocity. This is first explored in the time-averaged time scale, before attempting to link these measurements with observations of the geometry of individual waves.

Key words: LiDAR scanner, surf zone, wave asymmetry, skewness, wave-by-wave analysis

1. Introduction

In recent years, LiDAR scanners and remote sensors in general have been increasingly used for the monitoring of hydrodynamics and morphodynamics in the surf and swash zone (Brodie *et al.*, 2015; Almeida et *al.*, 2015; Martins et *al*, 2016). The advantages of remote sensors in this very dynamic region of the nearshore are numerous, but principally reside in the spatial extent and resolution of the measurements, the ease of deployment and the field maintenance. However, to measure wave geometries in field conditions, traditional remote sensors such as video cameras are limited by the need for *in-situ* probes (Almar et *al.*, 2012; Carini et *al.*, 2015) or specific processing that introduce difficult to quantify errors (Robertson et *al.*, 2014).

LiDAR scanners use the time-of-flight technique applied to light beams to measure the distance between the sensor and an object (Tamari et *al.*, 2011; Martins et *al.*, 2016). 2D scanners are therefore capable of measuring wave profile and their evolution assuming that a return signal from water surface is possible. In the surf zone, the presence of foam and air bubbles at the sea surface allows for an accurate detection of the surface through diffuse reflection (Blenkinsopp et *al.*, 2010; Brodie et *al.*, 2015; Martins et *al.*, 2016). In freshwater conditions, Blenkinsopp et *al.* (2012) accurately captured shoaling wave profiles with diffuse reflection at the surface by controlling the turbidity levels. The presence of particles under the surface also renders an estimation of the reservoir stage possible through the Tyndall effect (Tamari et *al.*, 2011).

A major advantage of LiDAR scanners for surf zone monitoring applications is that the directly measure time-varying surface elevation without signal correction or transformation after measurement. In surf zone field studies, wave transformation is generally measured using pressure transducers (Inch et *al.*, 2014), the data from which is transformed into surface elevation either using the hydrostatic hypothesis (*e.g.* Raubenheimer et *al.*, 1996), linear wave theory (*e.g.* Sallenger and Holman, 1985) or a combination of the two, depending on the transducer position in the surf zone (Sénéchal et *al.*, 2001). Bishop and Donelan (1987) demonstrated that linear wave theory was adequate to describe wave heights in the surf zone within 5% when using spectral estimates. However, Martins et *al.* (2017) observed discrepancies at the wave-by-wave scale of up to 30% of the wave height close to the break point. Furthermore, linear wave theory also failed to

accurately describe the temporal asymmetry of the wave profile.

For the first time, Brodie *et al.* (2015) presented LiDAR-derived wave-averaged asymmetry and skewness measurements in the surf zone, showing a favourable match with pressure-derived data. However, little is known about the geometrical characteristics of individual waves compared to these statistical quantities. Asymmetry in near-bed velocities is responsible for onshore sand transport under skewed waves (Elfrink et *al.*, 1999; Elgar et *al.*, 2001; Grasso et *al.*, 2011). The link between asymmetry at the surface and that at the bed started to be explored through the measurement of synchronized free surface elevation and current velocity data during high resolution laboratory experiments (Michalet et *al.*, 2011; Rocha et *al.*, 2017). The conclusion was that both parameters (especially the skewness) were overestimated when calculated from the surface measurements. However, the likely reasons for this are not very clear, nor the potential link with the wave geometry itself.

As part of the EPSRC-funded WASH project, three LiDAR scanners were deployed along the pier in Saltburn, UK, in order to obtain continuous free surface measurements of breaking waves over several wavelengths. This dataset allows for a very detailed description of the wave shape at the individual scale, and at various stage of its transformation: shoaling, breaking and propagation in the inner surf zone. Hydrodynamic measurements were also obtained from a series of Acoustic Doppler Velocimeters (ADV). In this paper, the geometry of broken and non-broken waves is studied at the individual and time-averaged scales. The link between the wave characteristics at the surface and the current velocities is explored. The objective is to draw simple relations between the two as it is often impossible to deploy *in-situ* instruments; in this situation a LiDAR could therefore provide indirect estimates of time-averaged near-bed velocities. Finally, while paramount for energy dissipation parameterization in numerical models, wave slopes are generally assumed to be constant throughout the surf zone. This new dataset shows that the wave angle varies with the local depth, and it is generally larger for the present conditions than is generally assumed.
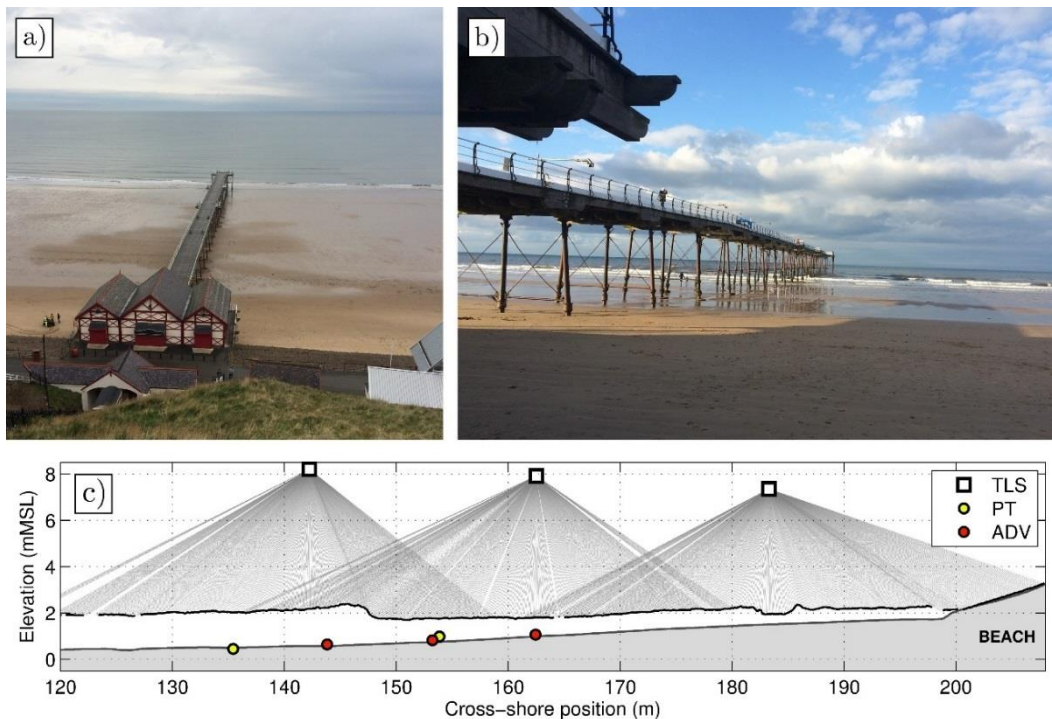

Figure 1: Presentation of the macrotidal site of Saltburn-by-the-Sea: a) aerial view and b) view from the beach, with visual on the LiDAR scanners. Panel c) shows a schematic of the set-up with an example of post-processed free surface elevation (black thick line while individual measurements are shown as light gray lines). The beach profile (thick gray line) corresponds to the surveyed profile during the previous low tide.
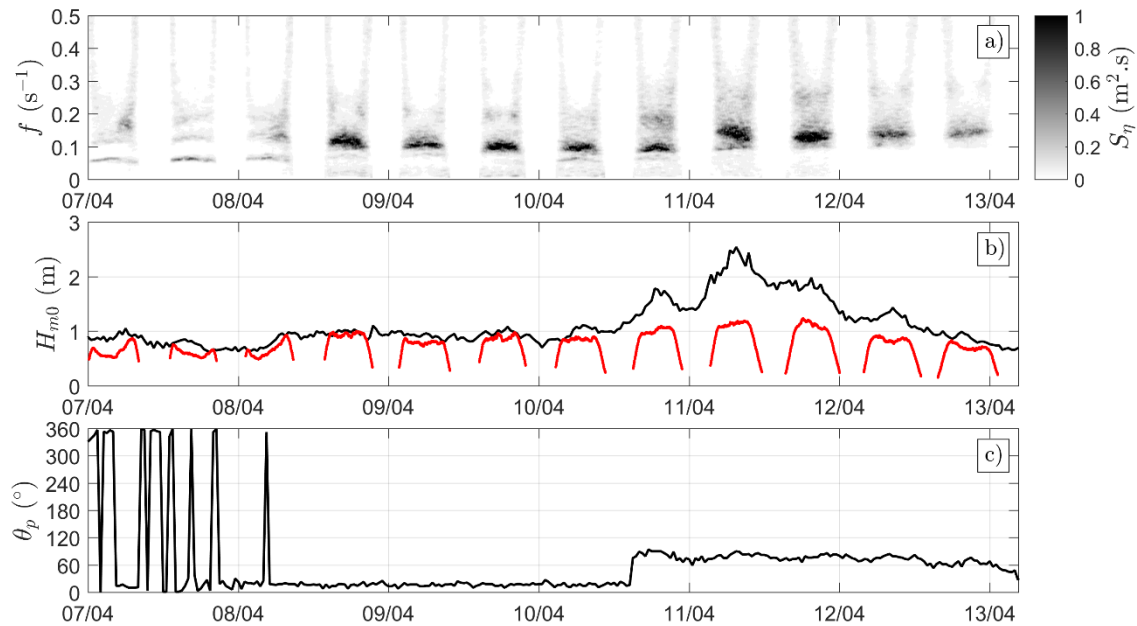
1443

Figure 2. Wave conditions during the experiments measured at the entrance of the pier by the 2 Hz pressure transducer (PT) and offshore: a) energy spectral density estimated by the PT over 24-m long moving windows; b) Significant .wave height measured by the PT (red dots) and by the Whitby buoy; c) Wave peak direction measured by the Whitby buoy.

2. Experimental set-up

2.1. *Field site and experimental setup*

The 206 m long historical pier at Saltburn-by-the-Sea (see Figure 1a-b) was used for the first WASH experiments between 7th April and 13th April 2016. Saltburn is situated on the North East coast of England, and experiences a macrotidal environment: the measured tidal range at the closest harbour (Whitby) reached a maximum of 5.42 m on 08/04 decreasing to 3.47 m on 13/04. This allowed for detailed LiDAR, GPS and total station surveys of the exposed beach at every low tide.

Three commercial 2D LiDAR scanners (SICK LMS511, λ = 904 nm) were deployed along the pier, cantilevered 2.5 m from the pier railing on scaffold poles (Figure 1b). Three RBR Pressure Transducers (PT) sampling at 2 Hz were deployed, two below the most seaward LiDAR scanners (Figure 1c), and one located at the offshore end of the pier to monitor the incident wave conditions. Additionally, three Nortek Acoustic Doppler Velocimeters (ADV) sampling at 16 Hz were deployed under the pier. Each was equipped with an internal pressure sensor, but the two most onshore ADVs were also synchronized with an external PT and Optical Backscatter Sensor (OBS).

2.2. *Wave conditions*

Figure 2 displays the wave conditions experienced during the experiments, measured by the PT at the offshore end of the pier. The period analysed here corresponds to the four tides from 09/04 and 10/04 April, with a clean swell from 20°NE ($T \sim 10 - 11$ s, $H \sim 0.9 - 1$ m, see Figure 2). As the orientation of the pier is roughly 18°NE, the propagation of the swell was parallel to the pier, which is ideal for the LiDAR scanner setup as it minimises interactions between the measured waves and the pier structure. Prior to these two days, conditions were less energetic and mainly infragravity-dominated (especially on 07/04, Figure 2a). From the second tide of 10/04, the wave energy spectrum started to spread, with a more locally generated sea from the East (Figure 2c).

1444

2.3. *Data Processing*

The procedure to process the data from the three LiDAR scanners during the Saltburn experiments is described in Martins et al. (2017), but a brief overview is given here. Each individual LiDAR scanner dataset underwent the series of transformation described in Martins et *al.* (2016) – translation, correction of the roll angle and spatial interpolation onto a 0.1 m regular grid. The three individual datasets were then merged into a unique surface elevation dataset, covering the whole surf zone. In the overlapping areas, linear weighing functions were used to prioritize the closest LiDAR scanner. An example of measured surface elevation is shown in Figure 1c, and illustrates the spatial resolution and coverage of the present dataset (over ~100 m of surf zone captured).

The pressure data used in this paper correspond to the data from the internal pressure sensor from the offshore ADV, and from the two external PTs at the middle and onshore ADV locations. Linear wave theory was used to correct for depth attenuation of the pressure signal (*e.g.* Bishop and Donelan, 1987). Although the limitations of this approach are known (see Introduction), the objective here is to compare the results obtained using this theory with the LiDAR measurements at various temporal scales. The ADV current data was processed following the procedure described in Mori et *al.* (2007).

3. Methods

3.1. *Time-averaged third order moments*

Wave skewness S_k and asymmetry A_s are a measure of nonlinearity, which can be used to characterise wave geometry in the surf zone. High skewness waves are characterized by a narrower crest and broader trough while highly asymmetric waves generally have a steep front and gradually sloping back, as is the case with broken waves (bores). For the surface elevation η, S_k and A_s are defined as follows:

$$S_k = \frac{\overline{(\eta(t)-\overline{\eta})^3}}{\overline{(\eta(t)-\overline{\eta})^2}^{3/2}} \tag{1}$$

$$A_s = \frac{\overline{Im(H(\eta(t)-\overline{\eta}))^3}}{\overline{(\eta(t)-\overline{\eta})^2}^{3/2}} \tag{2}$$

where $Im(H(.))$ is the imaginary part of the Hilbert transform and $\overline{.}$ is the time-averaged operator (Berni et *al.*, 2013).

The wave skewness and asymmetry were calculated for both pressure-derived and LiDAR η measurements, using 20 minute-long data windows. Similarly, the skewness and asymmetry of the cross-shore bottom current velocity u measured at the three cross-shore locations were calculated (replacing η by u in Equations 1 and 2). In that way, skewness and asymmetry at the surface can be related to that of the current close to the bottom.

3.2. *Individual definitions for wave skewness and asymmetry*

To study the geometrical properties of individual waves, a temporal framework needs to be defined. Here we use the definition of an individual wave described in Martins et *al.* (2016, 2017): waves are detected as peaks in the surface elevation timeseries, and the two surrounding troughs are also extracted. At a certain cross-shore location, the wave height H is defined as the elevation between the crest and the preceding trough. The wave period T is then defined as the time elapsed between the detection of the two surrounding troughs at this location. Following the approach of Martins et *al.* (submitted), using the definitions of Cowell (1982) and Adeyemo (1968), we can define individual wave skewness and asymmetry. Figure 3 shows the definition of the different individual wave properties used for estimate these parameters; these are as follows:

- the crest elevation η_c above a mean water level (*MWL*)
- the wave height H
- the wave period T
- the wave front angle θ_{front}, estimated between the wave crest and the first detected measurement point 65% of H below the crest

- the wave back angle θ_{back}, estimated between the wave crest and the first detected measurement point 65% of H below the crest
- the time elapsed t_a between the moment the surface up-crosses MWL and the crest detection moment
- the time elapsed t_b between the moment the surface down-crosses MWL and the crest detection moment

At the individual time scale, the definition of a MWL is a critical aspect because of the presence of infragravity waves (Power et al., 2010; Martins et al., 2016). For geometrical purposes, the MWL that makes most sense is the period-averaged water depth h_w (surface elevation averaged over the individual wave period). The following wave properties were extracted:

$$D = t_a/t_b \qquad (3)$$

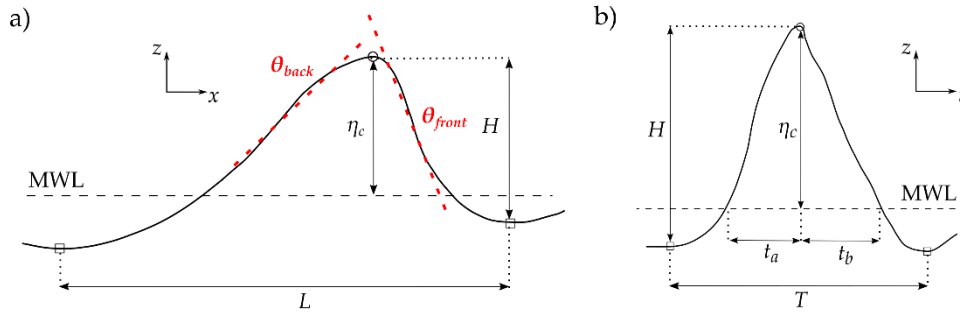$$A_s = 2(t_a + t_b)/T \qquad (4)$$

$$S_k = 2\eta_c/H - 1 \qquad (5)$$

Figure 3: Spatial (panel a) and temporal (panel b) definition of wave individual properties, used for the definition of individual wave skewness and asymmetry (Equations 3, 4 and 5).

4. Time-averaged third moments parameters

4.1. *Relation between surface and bottom cross-shore velocity*

The present paper focuses on data from the periods roughly 2 hours either side of high tide during 09/04 and 10/04, 4 high tides in total. Figure 4 shows the comparison of the significant wave height H_{m0}, wave asymmetry A_s and skewness S_k measured by the LiDAR and pressure transducers at the three ADV locations (Figure 1). These parameters were calculated using moving windows of 20 minutes, to allow for a more continuous description throughout the tide. A threshold of 75% non-NaN values over that window was used for the LiDAR dataset. This explains that some data are missing at high tide, when there was less consistent wave breaking over the two most offshore ADV.

The significant wave height measured by the PT and LiDAR show very good agreement (Figure 4a, 4d and 4g), at every location and every stage of the tide. This is consistent with the results from Brodie et al. (2015) who obtained similar results in their field dataset. Despite the probable significant differences between pressure-derived and the real wave height at the wave-by-wave scale (Martins et al., 2017), the spectral parameters present good agreement, consistent with the conclusion of Bishop and Donelan (1987).

Comparison of time-averaged wave asymmetry from the PT and LiDAR (Figure 4b, 4e and 4h) also show excellent agreement at all stages of the tide. During the flooding and ebbing period (wave height to water depth ratio $\gamma \in [0.45; 0.55]$), A_s exhibits a peak value and then decreases to reach its minimum values around high tide. However, the wave skewness estimated from the LiDAR scanner is consistently greater than that estimated from the pressure-derived signal (a very good correlation is found for the relation $S_{k,LiDAR} = 1.2 S_{k,PT}$, $r = 0.9$ and Scatter Index of 0.07). Considering the physical explanation that is given to the wave skewness, a possible explanation at this stage of the analysis could be that the underestimation of individual wave height in the pressure-derived dataset at the onset of breaking or soon after affect the time-averaged parameter. This will be discussed in section 6.
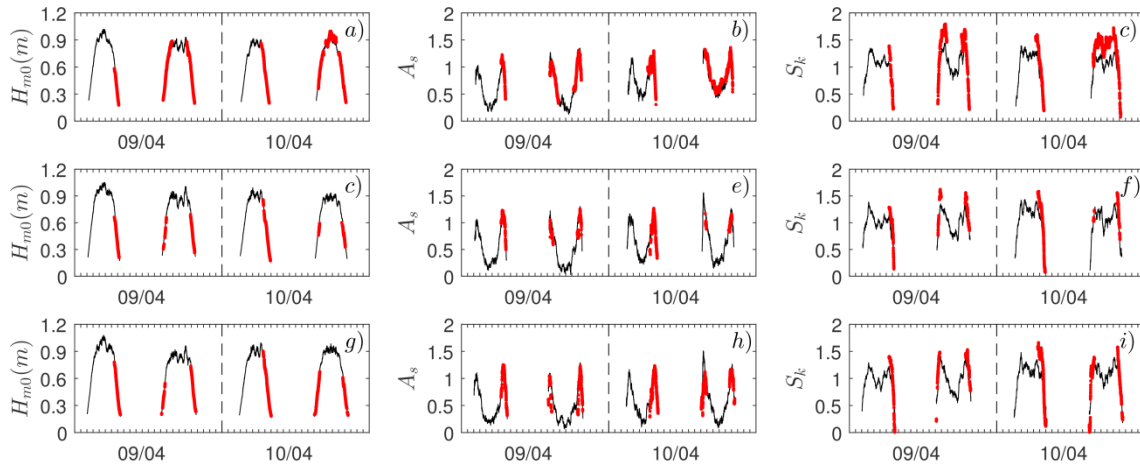
Figure 4: Comparison between pressure-derived (black line) and LiDAR (red points) of significant wave height H_{m0}, wave asymmetry A_s and skewness S_k. Panels a-c) show the data at the onshore ADV location ($x = 162$ m), while panels d-f) and g-i) show the data at the middle ($x = 153$ m) and offshore ($x = 144$ m) ADV locations respectively.

4.2. *Relation between surface and bottom cross-shore velocity*

Wave skewness and asymmetry (Equations (1) and (2) respectively) estimated from the surface elevation η and bottom current velocity u were compared to investigate the possibility of predicting the third-moments of the cross-shore current velocity from the surface signal.

Two different comparisons were performed: 1) A_s and S_k compared with no specific processing on η or u; 2) A_s and S_k compared with a Fourier low-pass filter on η, with the cutoff frequency chosen as three times the peak frequency. This was attempted as Berni et *al.* (2013) showed that three Fourier components were enough to accurately describe the free-stream velocity under skewed and asymmetric waves.

The results are first displayed in Figure 5 as a timeseries for the data from the offshore ADV location. It is observed that during the four tides of interest (09/04 and 10/04), the asymmetry and skewness calculated from the filtered surface elevation signal is in better agreement than when estimated with the full η spectrum. The major improvements principally concern the periods when the water is relatively shallow (flooding and ebbing), where due to the presence of bores, S_k presents values of up to twice that at high tide, and up to ten times for A_s.

The ADV data (with and without frequency cutoff) as well as the LiDAR data (with frequency cutoff) from every cross-shore location and all tides are displayed in Figure 6. It is shown that the wave asymmetry and skewness estimated from the filtered surface elevation derived from PTs and LiDARs closely match those for the bottom current velocity. For the ADV data, besides the fact that the mean points estimated from the filtered signal are closer to the 1:1 line, standard deviations are also smaller. Considerable deviation between these filtered signal datasets and the current velocity dataset is still observed for very low values of A_s ($A_s < 0.1$) and especially very low values of S_k ($S_k < 0.15$), although there is considerable scatter for these ranges of values. This suggests that at low tide (Figure 5), both the cross-shore current asymmetry and skewness will typically be underestimated when based on the surface asymmetry. The presence of strong infragravity waves observed at this stage of the tide could explain this phenomenon.
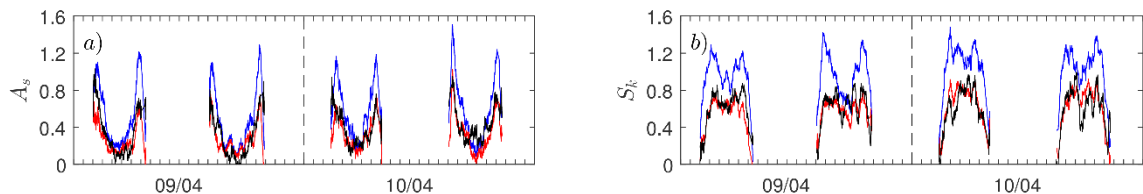

Figure 5: Timeseries comparison of third-order wave moments data estimated from pressure and velocity measurements from the offshore ADV location: panel a) shows $A_{s,u}$ (black line) against $A_{s,\eta}$ based on the full spectrum of η (blue line) and $A_{s,\eta}$ based on the η with a cutoff frequency of $3f_p$ (red line); panel a) shows $S_{k,u}$ (black line) against $S_{k,\eta}$ based on the full spectrum of η (blue line) and $S_{k,\eta}$ based on the η with a cutoff frequency of $3f_p$ (red line).
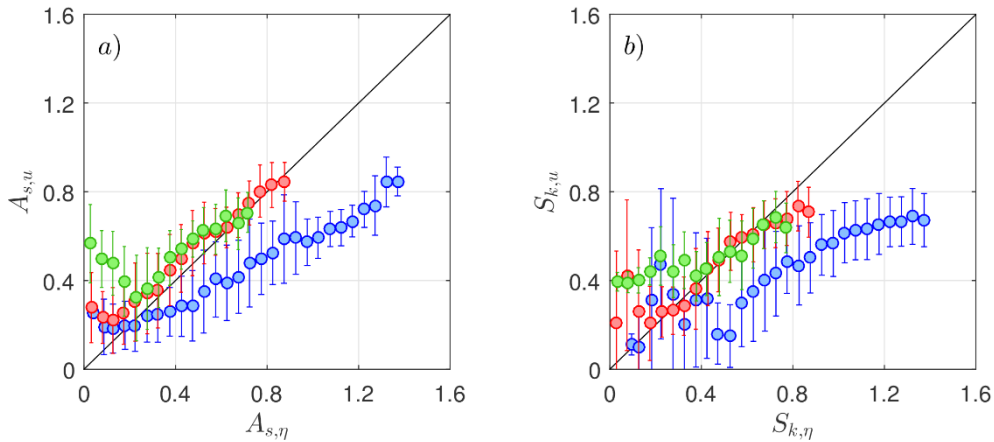
1447

Figure 6: Comparison of all third-order wave moments data estimated from LiDAR, pressure and velocity measurements: panel a) shows $A_{s,u}$ against $A_{s,\eta}$ while panel b) shows $S_{k,u}$ against $S_{k,\eta}$. In each subplot, red dots correspond to data from the ADV using the frequency cutoff on η, while the full spectrum was used for the blue data. Green data correspond to the LiDAR scanner, with the same frequency cutoff. Bins of 0.05 in the x-direction were used to calculate the mean and standard deviation, represented as error bars. The 1:1 line is shown as black line.

5. Wave-by-wave analysis of wave skewness and asymmetry

To further compare the pressure, velocity and surface elevation datasets, a wave-by-wave analysis has been performed on the pressure-derived and LiDAR surface elevation signals, and on the cross-shore current velocity signal (Section 3.2). The analysis presented here focuses on the data obtained at the onshore ADV location. Figure 7 displays the different parameters studied: D, A_s and S_k (Equation 3-5), along with the front and back wave angles θ_{front} and θ_{back}. For each property, the mean was computed using moving windows of 60 waves, and the shaded area represents the standard deviation over the 60 waves.

The first observation that can be made is that there is a general good agreement between all datasets, for every tide (Figure 7a-c). Especially, the mean individual wave properties extracted from surface or the current velocity signal show good correlation, without the need of a frequency low-pass filter for the surface elevation. The wave deformation D presents very similar values over the course of the experiments (Figure 7a): values generally range from 0.3 at low tide and increase to 0.8-0.9 at high tide. Values from the LiDAR scanner present more scattered data at high tide probably because it detects a broader range of surface wave frequencies. At high tide, the presence of very short waves along with longer non-broken waves makes the range of values reached by D greater.

The wave-by-wave asymmetry presents less scatter than other properties (Figure 7b), but there is more divergence between the datasets. Consistent with its definition (Equation 4) and the evolution of D, A_s based on surface elevation increases to values around 0.8 at high tide. This means that over the wave period, there is less difference between the time elapsed by the surface elevation above h_w than under. During ebb or flooding, A_s decreases: the crest is narrower (in time) compared to the trough. This narrowness does not appear in the current velocity-derived A_s that present more constant values. This could be explained by the presence of infragravity waves: although their influence on the surface elevation is reduced by using the local definition of h_w, they more strongly influence the underlying current.

The wave-by-wave skewness displays some interesting features (Figure 7c), especially during the second tide of 09/04. It is low in shallow waters (low tide) even in the presence of infragravity waves thanks to the use of h_w, and show peak values at some time during both flood and ebb periods, before decreasing at high tide. Similar behaviour was observed for the time-averaged A_s (Figure 4b, 4e and 4h). The breaking regime explains this behaviour, and it is illustrated in Figure 7d and 7e, with the measured front and back wave angles. The peaks in S_k coincide with a net increase in the back wave angle and a slight increase in the values and the amount of scatter of the front angle: we pass from the presence of only broken waves, to a regime where wave breaking occurs at this location. It is noteworthy that the mean front wave angles are larger than found in the literature (*e.g.* Carini *et al.*, 2015).
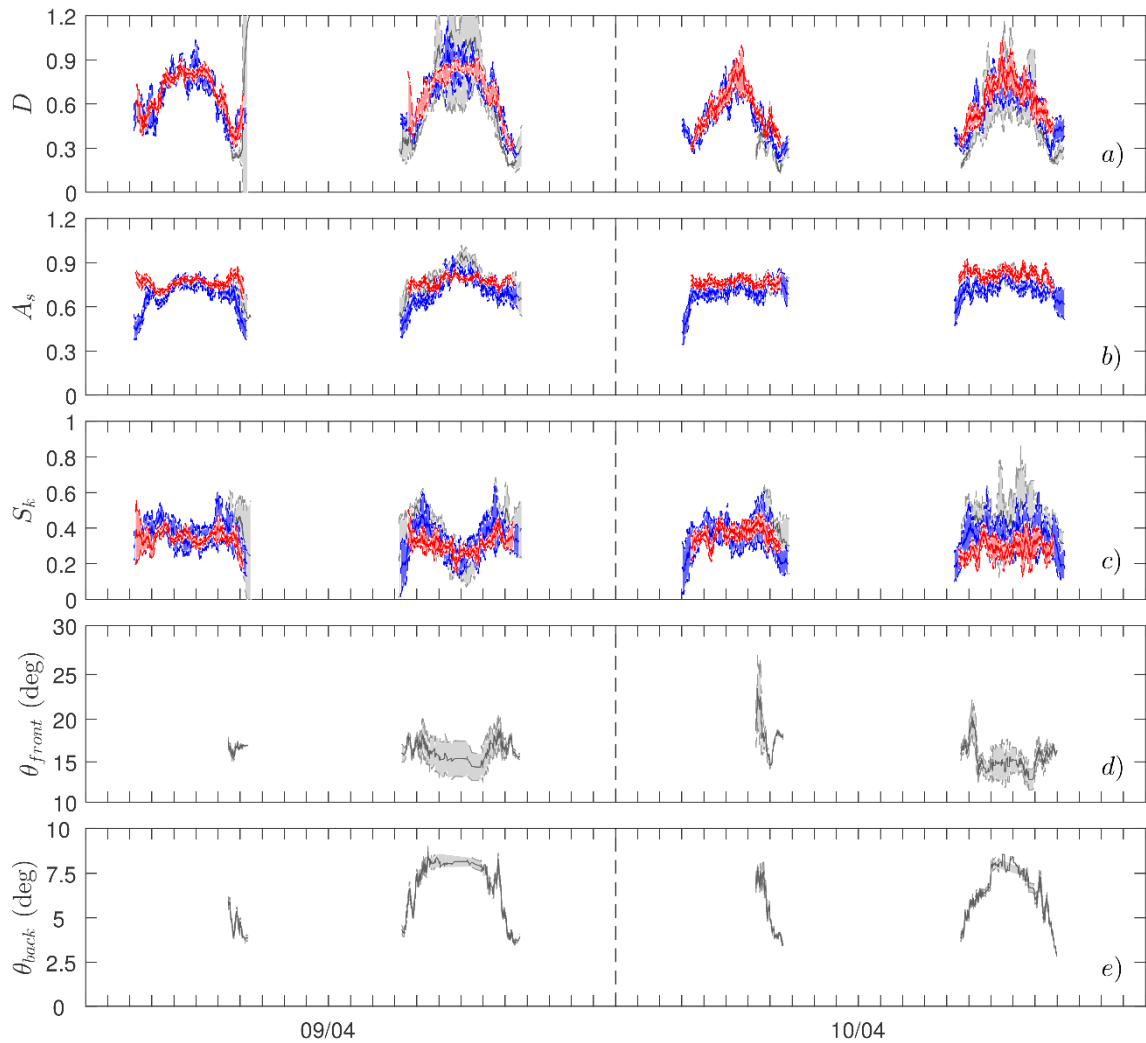
Figure 7: Comparison between pressure-derived and LiDAR data at the wave-by-wave scale: wave deformation D, wave asymmetry A_s and skewness S_k. Panels d-e) show the individual wave front and back angles respectively. For each wave properties, the mean (continuous line) is calculated using a moving window of 60 waves, and she shaded area correspond to the standard deviation. Pressure-derived data is shown as blue, current data is shown as red and LiDAR data is shown as gray.

6. Potential of LiDAR technology to retrieve cross-shore current velocity third-order moments

The results presented in Section 4.2 show that it is possible to estimate free-stream velocity skewness and asymmetry from surface elevation measurements. These results also confirm the observations from Berni et al. (2013) that only three Fourier components are needed to correctly reproduce the free-stream current velocity.

The fact that the third-order wave moments, estimated from the LiDAR and pressure-derived surface elevation datasets, correlate well opens up promising applications for coastal monitoring (something already pointed out by Brodie et al., 2015). With a single scanner deployed nearshore, one can estimate cross-shore current velocity third-order moments during energetic events and then correlate these to the morphological change. Data from the scanner with the same frequency cutoff as that used for the ADV are also shown in Figure 6 and support this suggestion.

An example of this application from the present dataset is displayed in Figure 8. As the experiment was designed to focus around mid-tide, the wave parameters (A_s and S_k) are not calculated for other periods since no consistent breaking was observed at high tide for most of the measured area. However, it still give some insights of the cross-shore and temporal variability of the time-averaged parameters. As observed before, the
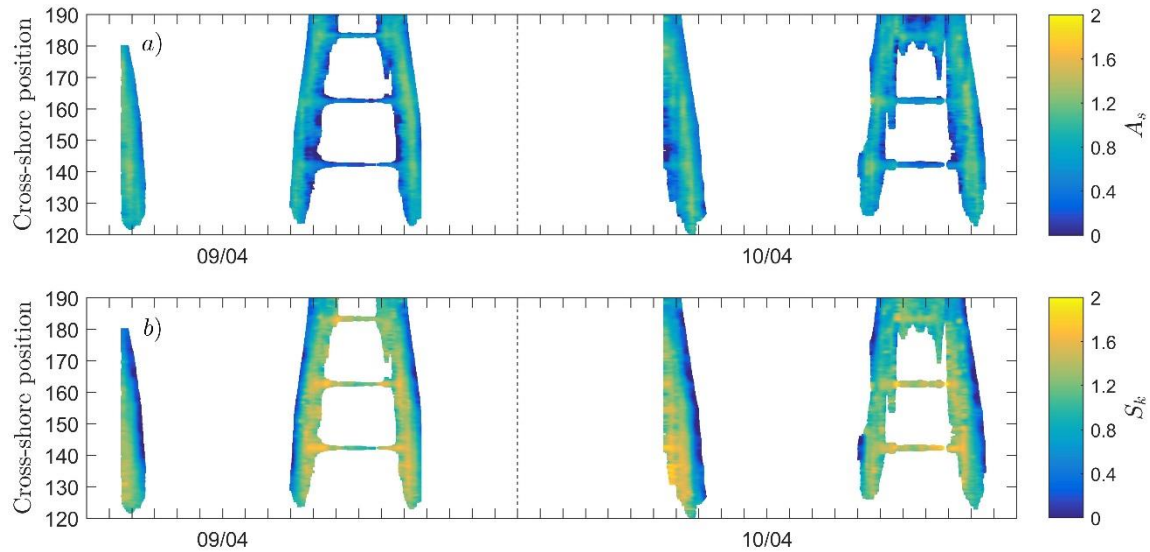
Figure 8: Timestack of time-averaged wave asymmetry A_s (panel a) and skewness S_k (panel b): time-evolution of the parameters against the cross-shore position.

wave asymmetry seems to exhibit the highest values when strong breaking occur (yellow in Figure 8a), and then decreases towards shore. It then diminishes when the local water depth increases (flooding period). The wave skewness is more monotonic: higher values are observed for deeper water and it then decrease toward the shore (Figure 8b). Globally, both parameters are found relatively constant in time at the same stage of the tide, and this may explain the small changes in bed morphology observed during these two days.

The cutoff frequency used on the surface elevation signal to accurately estimate the third-order current velocity moment is a sensitive point. Figure 4c, 4f and 4i suggest that depending on the presence of short waves at the surface, and possibly the sampling rate of the sensors, the estimates of S_k can be affected. The frequency cutoff of three Fourier components worked well in laboratory conditions for Berni et al. (2013), and in field conditions here, but this is probably because most of the energy was contained within these frequencies for this case. This corroborates with the spectral shapes observed (Figure 2a). For a much wider spectrum or in more infragravity-dominated conditions, it is uncertain whether the same cutoff would be appropriate.

7. Conclusion

During these experiments, three LiDAR scanners were deployed along a pier to generate a unique surface elevation dataset of shoaling, breaking and broken waves. In the present study, a link between the wave-by-wave and the time-averaged scales is found. The wave-by-wave parameters estimated on the pressure-derived, current velocity and LiDAR datasets are consistent with expected results throughout the tide cycle. The wave-by-wave skewness is the parameter at the individual wave scale that relates the most to time-averaged parameters, and in particular to the wave asymmetry A_s. The presence of noise and waves with a frequency greater than the peak frequency in the surface elevation signal was found to increase the time-averaged skewness. A frequency cutoff of three times the peak frequency applied to the surface elevation enables good estimates of the third-order cross-shore current velocity moments. This opens up the possibility for interesting LiDAR applications for the remote sensing of third-order moments of nearshore current. Finally, the LiDAR provides the possibility to measure the surface slopes of surf zone waves. For this particular dataset, the angles measured at the front are larger than the values usually used in numerical models of nearshore circulation. Further analysis is required to understand the link to between surface slope and wave properties, but provides the potential to give improvements in such modelling.

Acknowledgements

References

Adeyemo, M., 1968. Effect of beach slope and shoaling on wave asymmetry. Coastal Engineering Proceedings, 1(11).

Almeida, L.P., Masselink, G., Russell, P.E., Davidson, M.A., 2015. Observations of gravel beach dynamics during high energy wave conditions using a laser scanner. Geomorphology (228), pp. 15-27, ISSN 0169-555X. doi:10.1016/j.geomorph.2014.08.019.

Berni,C., Barthélemy, E, Michallet, M., 2013. Surf zone cross-shore boundary layer velocity asymmetry and skewness: An experimental study on a mobile bed, Journal of Geophysical Research: Oceans (118), pp. 2188-2200. doi:10.1002/jgrc.20125.

Bishop, C.T., Donelan, M.A., 1987. Measuring waves with pressure transducers, Coast. Eng. (11), pp. 309–328. doi:10.1016/0378-3839(87)90031-7.

Blenkinsopp, C.E., Mole, M.A., Turner, I.L., Peirson, W.L., 2010. Measurements of the timevarying free-surface profile across the swash zone obtained using an industrial (lidar), Coast. Eng. (57), pp. 1059–1065. doi:10.1016/j.coastaleng.2010.07.001

Brodie, K.L., Raubenheimer, B., Elgar, S., Slocum, R.K., McNinch, J.E., 2015. Lidar and pressure measurements of inner-surfzone waves and setup, Journal of Atmospheric and Oceanic Technology (32), pp. 1945-1959. doi:10.1175/JTECH-D-14-00222.1.

Carini, R.J., Chickadel, C.C., Jessup, A.T., Thomson, J., 2015. Estimating wave energy dissipation in the surf zone using thermal infrared imagery, Journal of Geophysical Research: Oceans (120), pp. 3937-3957. doi:10.1002/2014JC010561

Cowell, P.J., 1982. Breaker stages and surf structure on beaches, Coastal Studies Unit Technical Report No. 82/7, Sydney, Australia.

Duncan, J.H., 1981. An Experimental Investigation of Breaking Waves Produced by a Towed Hydrofoil. Proc. R. Soc. Lond. A 377 331-348. doi:10.1098/rspa.1981.0127.

Elfrink, B., Rakha, K.A., Deigaard, R., Brøker, I., 1999. Effect of near-bed velocity skewness on cross shore sediment transport, in: Proceedings of the 4th International Symposium on Coasting Engineering and Science of Coastal Sediment Processes (ASCE), Hauppauge, New York, United States, pp. 33–47.

Elgar, S., Gallagher, E.L., Guza, R.T., 2001. Nearshore sandbar migration, J. Geophys. Res.: Ocean. (106), pp. 11623–11627. doi:10.1029/2000JC000389.

Grasso, F., Michallet, H., Barthélemy, E., 2011. Sediment transport associated with morphological beach changes forced by irregular asymmetric, skewed waves, J. Geophys. Res.: Ocean. (116). doi:10.1029/ 2010JC006550.

Inch, K., 2014. Surf zone hydrodynamics: Measuring waves and currents, in: Geomorphological Techniques, Chap. 3, Sec. 2.3, British Society of Geomorphology.

Martins, K., Blenkinsopp, C.E., Zang, J., 2016. Monitoring Individual Wave Characteristics in the Inner Surf with a 2 Dimensional Laser Scanner (LiDAR). Journal of Sensors, vol. 2016. doi:10.1155/2016/7965431.

Martins, K., Blenkinsopp, C.E., Almar, R., Zang, J., 2017. The influence of swash-based reflection on surf zone hydrodynamics: a wave-by-wave approach, Coast. Eng. (122), pp. 27-43. doi:10.1016/j.coastaleng.2017.01.006.

Martins, K., Blenkinsopp, C.E., Power, H.E., Bruder, B., Puleo, J.A., Bergsma, E.W.J. High-resolution monitoring of wave transformation in the surf zone using a LiDAR scanner array, submitted to Coast. Eng.

Michallet, H., Cienfuegos, R., Barthélemy, E., Grasso, F., 2011. Kinematics of waves propagating and breaking on a ba rred beach, European Journal of Mechanics B/Fluids (30), pp. 624-634. doi:10.1016/j.euromechflu.2010.12.004.

Mori, N., T. Suzuki and S. Kakuno, 2007. Noise of acoustic Doppler velocimeter data in bubbly flow, Journal of Engineering Mechanics, American Society of Civil Engineers (133), pp.122-125. doi:10.1061/(ASCE)0733-9399(2007)133:1(122).

Raubenheimer, B., Guza, R.T., Elgar, S., 1996. Wave transformation across the inner surf zone, Journal of Geophysical Research: Oceans (101), pp. 25589–25597. doi:10.1029/96JC02433.

Rocha, M.V.L., Michallet, H., Silva, P.A., 2017. Improving the parameterization of wave nonlinearities – The importance of wave steepness, spectral bandwidth and beach slope, Coast. Eng. (121), pp. 77-89. doi:10.1016/j.coastaleng.2016.11.012.

Sallenger Jr., A.H., Holman, R.A., 1985. Wave Energy Saturation on a Natural Beach of Variable Slope, Journal of Geophysical Research: Oceans (90), pp. 11939-11944. doi:10.1002/jgrc.20125.

Sénéchal, N., Dupuis, H., Bonneton, P., Howa, H., Pedreros, R., 2001. Observation of irregular wave transformation in the surf zone over a gently sloping sandy beach on the French Atlantic coastline, Oceanologica Acta (24), pp. 545–556, 2001. doi:10.1016/S0399-1784(01)01171-9.

Tamari, S., Mory, J., Guerrero-Meza, V., 2011. Testing a near-infrared Lidar mounted with a large incidence angle to monitor the water level of turbid reservoirs, ISPRS Journal of Photogrammetry and Remote Sensing (66), pp. S85-S91. doi:10.1016/j.isprsjprs.2011.01.009.